Facilitating low energy activation in the near-infrared long-afterglow complex spinel Zn1+xGa2-2xSnxO4:Cr 3+ via band gap engineering and control of cation occupancy

Zaifa Pan, Victor Castaing, Liping L Yan, Lulu Zhang, Cong Zhang, Kang Shao, Yifan Zheng, Changkui Duan, Jianhua Liu, Cyrille Richard, et al.

Article type: Full Paper

Facilitating low energy activation in the near-infrared long-afterglow complex spinel $Zn_{1+x}Ga_{2-2x}Sn_xO_4:Cr^{3+}$ *via* band gap engineering and control of cation occupancy

Zaifa Pan[†,], Victor Castaing[†], Liping Yan, Lulu Zhang, Cong Zhang, Kang Shao, Yifan Zheng, Changkui Duan, Jianhua Liu, Cyrille Richard, Bruno Viana**

Prof. Z.F. Pan, L.P. Yan, L.L. Zhang, C. Zhang, Dr. K. Shao

College of Chemical Engineering, Zhejiang University of Technology, Hangzhou 310014, P.R. China

E-mail: panzaifa@zjut.edu.cn

Prof. Y.F. Zheng

Research Center of Analysis and Measurement, Zhejiang University of Technology, Hangzhou 310014, P.R. China

Prof. C.K. Duan

Key Laboratory of Strongly-Coupled Quantum Matter Physics, Chinese Academy of Sciences, School of Physical Sciences, University of Science and Technology of China, Hefei 230026, P. R. China

V. Castaing, Prof. B. Viana

PSL Research University, Chimie ParisTech − CNRS,

Institut de Recherche de Chimie Paris, 75005 Paris, France,

E-mail: bruno.viana@chimie-paristech.fr

J. Liu, Dr. C. Richard

Unité de Technologies Chimiques et Biologiques pour la Santé, Université Paris Descartes, CNRS UMR8258, INSERM U1267, Paris, France

Keywords: persistent luminescence, complex spinel, low energy activation, band gap engineering, cation occupancy control

ABSTRACT

Cr^{3+} activated persistent luminescent phosphors with the spinel structure, and particularly $ZnGa_2O_4:Cr^{3+}$, are attracting a great deal of attention for their distinctive deep red persistent emission and their potential bio-imaging applications. The exploration of new spinel host lattices has the potential to produce new superior persistent luminescence materials by optimization of the emission and trapping properties. Here, we report the detailed optical characterization of a series of near-infrared long-afterglow materials with nominal formula $Zn_{1+x}Ga_{2-2x}Sn_xO_4:Cr^{3+}$, which have been synthesized by high temperature solid-state methods. The variation of crystal field strength and band gap energies causes both the persistent luminescence excitation and emission (Cr^{3+}: $^4T_2 \rightarrow {}^4A_2$ band) spectra of the optimized complex spinel samples to be redshifted compared to the normal spinel $ZnGa_2O_4:Cr^{3+}$. The persistent emission redshift is of interest for improved deep tissue penetration, whereas the persistent excitation redshift facilitates the activation of the persistent luminescence by low energy radiation. Furthermore, it appears that increasing the rate of cation site-inversion in the spinel can lead to an optimum anti-site defect concentration for charge trapping. These results, which highlight the benefit of cation occupancy control for persistent luminescence properties, may be of further interest for the development of spinel materials with optimized optical properties.

1.Introduction

Persistent luminescent materials are attracting a great deal of attention in bio-imaging applications, because they feature an inherent advantage over conventional luminescent materials that require constant *in situ* excitation.[1-4] This feature not only suppresses photodamage of biological tissue from external excitation light, but also reduces autofluorescence background,[5] leading to ultrahigh signal-to-noise ratio. Furthermore, due to the deep penetration of near infrared (NIR) photons in bio-tissues, persistent luminescent materials with NIR emissions are particularly suitable for deep tissue imaging.[1-7] Cr^{3+} activated phosphors with the spinel structure are currently the most promising materials for such applications, due

to the suitable afterglow wavelength of Cr^{3+} (in the 650 - 750 nm emission range) and the high concentrations of antisite defects that are supported by the spinel lattice.

The normal spinel $ZnGa_2O_4:Cr^{3+}$ was reported as a new bright red persistent luminescent phosphor in 2011. The potential of its deep red persistent luminescence for application in *in vivo* imaging was demonstrated using activation by visible light (orange/red LEDs).[7,8] It is reported that the afterglow originates mainly from distorted Cr^{3+} and that antisite defects in the spinel lattice play a crucial role in the trapping mechanisms. However, the afterglow performance of $ZnGa_2O_4:Cr^{3+}$ is still too low for practical application. In the race for new persistent luminescent materials for *in vivo* applications, a considerable amount of research on the persistent emission and trap tuning by aliovalent substitution,[9] co-doping[10-14] and lattice modification of the spinel host is still in progress. [15-18]

The red persistent luminescence of this spinel phosphor was improved considerably by the aliovalent substitution of gallium by germanium or tin, with a nominal composition $Zn_{1+x}Ga_{2-2x}(Ge/Sn)_xO_4 (0 \leqslant x \leqslant 0.5)$.[9] Such aliovalent substitutions (in this case the replacement of a trivalent cation by tetravalent one) induces distorted octahedral sites in the resulting spinel solid solutions, which are surrounded by octahedral Ge/Sn positive defects, and work as new efficient traps. Similarly, the new partially Ge-substituted host, $Zn_3Ga_2Ge_2O_{10}:0.5\%Cr^{3+}$ presents a great enhancement of the NIR persistent luminescence, which can glow for more than 360 hours and can be repeatedly charged by sunlight.[15] New tin containing spinel host $Zn_3Ga_2SnO_8:0.5\%Cr^{3+}$[17] and Al doped non-gallate long-persistence phosphors $Zn_{2-x}Al_{2x}Sn_{1-x}O_4:0.2\%Cr^{3+}$[18] have also been designed. Both of these show remarkable long persistent luminescence properties with the potential for reproducible tissue imaging applications. Finally, a further enhancement of the persistent luminescence was obtained in Pr^{3+}/Cr^{3+} co-doped zinc gallogermanate $Zn_3Ga_2Ge_2O_{10}:Cr^{3+},Pr^{3+}$ and applied to long-term *in vivo* targeted tumor imaging, after bioconjugation with the peptide c(RGDyK).[10]

Spinels are conventionally represented by the formula AB_2O_4, in which element A is a divalent cation occupying a four-coordinate tetrahedral site and B is a trivalent cation occupying a six-coordinate octahedral site.[19,20] Consequently, a normal spinel can be described as $(A)[B]_2O_4$, where parentheses () and brackets [] denote tetrahedral and octahedral sites, respectively. In addition to the normal spinel structure, the valence state of the cations can be tetravalent and divalent, for example in $TiMg_2O_4$ and $TiZn_2O_4$[21,22] which are inverse spinels. In the inverse spinel structure, all the tetravalent cations (M) and half of the divalent cations (N) occupy octahedral sites, while the rest of the divalent cations (N) occupy tetrahedral sites. The general structure of inverse spinel compounds can be represented by the formula $(N)[MN]O_4$. It should be pointed out that intermediate occupancies (partial disordering of cations between the sites) are commonly observed with inverse cation distributions, which can be written as $(A_{1-x}B_x)[A^x_{/2}B_{1-x/2}]_2O_4$. For instance, the $ZnGa_2O_4$ host contains ~3% antisite defects.[9,18] Thanks to their distinctive antisite defects, spinel compounds are the most important hosts for near infrared long afterglow luminescent materials.[7] It is expected that site inversion will be more abundant in these intermediate occupancy compounds than those of pure normal spinel hosts.

Because of this structural chemistry, new complex spinels designed with intermediate site occupancies have the potential to host high concentrations of antisite defects, leading to better afterglow properties. Hence, a series of near infrared afterglow materials, comprised of complex spinels with different ratios of spinel $ZnGa_2O_4$ and inverse spinel Zn_2SnO_4, were targeted and prepared by a high temperature solid state method. The crystal structures and cation site occupancies were characterized by X-ray powder diffraction (XRD), transmission electron microscopy (TEM) and X-ray photoelectron spectroscopy (XPS). The effects of the band gap and traps on the afterglow properties in different hosts were studied by PL and PLE spectra, persistent luminescence excitation spectra, thermoluminescence curves and photon counting imaging. This detailed optical characterization demonstrates that these new complex spinel persistent luminescence materials are

more suitable for *in vivo* imaging through low energy activation. The evolution of the optical properties as a function of composition are discussed and illustrated with a series of schematic energy level diagrams.

2.Experimental

2.1. Sample preparation

The complex spinels were designed as combinations of the normal spinel $ZnGa_2O_4$ and inverse spinel Zn_2SnO_4 with different ratios, as represented by the formula $Zn_{1+x}Ga_{2-2x}Sn_xO_4:Cr^{3+}$ (x = 0.09, 0.11, 0.14, 0.20, 0.33, 0.5, 0.66 and 0.8, which we denote as ZGSO-2, ZGSO-3, …, and ZGSO-8). $ZnGa_2O_4$ (ZGO-1) and Zn_2SnO_4 (ZSO-9) were also prepared for comparison. The specific chemical composition of each sample is listed in **Table 1**. The doping content of activator Cr^{3+} is 0.5 mol % versus Ga^{3+} for all Ga containing samples and 0.5 mol % for the Zn_2SnO_4 sample. The powder samples were synthesized by a high-temperature solid-state method starting from binary oxide materials: ZnO (99.99%), Ga_2O_3 (99.99%), SnO_2 (99.99%), and Cr_2O_3 (99.99%). These starting materials were weighed according to the stoichiometric ratio of the formula. The mixed powders were ground homogenously in an agate mortar, and then the mixtures were put into an alumina crucible. The alumina crucible was subsequently placed in a high temperature furnace at 1350 ℃ for 9 h in air to produce the final samples. After cooling to room temperature, the phosphors were ground to a fine powder.

Table 1. Chemical compositions of complex spinels with different ratios of $ZnGa_2O_4$ and Zn_2SnO_4.

Samples	$ZnGa_2O_4:Zn_2SnO_4$	$Zn_{1+x}Ga_{2-2x}Sn_xO_4:Cr^{3+}$
ZGO-1	1:0	x = 0
ZGSO-2	10:1	x = 0.09
ZGSO-3	8:1	x = 0.11
ZGSO-4	6:1	x = 0.14
ZGSO-5	2:1	x = 0.33
ZGSO-6	1:1	x = 0.5

ZGSO-7	1:2	x = 0.66
ZGSO-8	1:4	x = 0.8
ZSO-9	0:1	x = 1

2.2. Characterization

The crystal structures and phase purities of the samples were characterized by PXRD using a PANalytical X'Pert Pro diffractometer with Cu Kα radiation, operating at 40 mA and 40 kV in the 2θ range from 5° to 125°, with a scanning step of 0.0167°. High-resolution transmission electron microscopy (HRTEM) micrographs, selected area electron diffraction (SAED) patterns and elemental mapping analysis were operated under a high-angle annular dark field mode by scanning transmission electron microscope (STEM, FEI Tecnai G2 F30 S-TWIN) with an accelerating voltage of 300 kV. XPS measurements were performed using an Axis Ultra DLD spectrometer (Kratos Analytical). The instrument was equipped with a monochromatized aluminium X-ray source powered at 15 kV and 3 mA, which delivered an X-ray beam of 300 μm × 700 μm. Charge compensation was obtained with a built-in charge neutralization system. The pass energy was set to 160 eV for both the survey spectra and the high-resolution spectra, and the pass energies of Zn 2p, Zn LMM Auger line, Ga 2p, O 1s and Sn 3d were 20 eV, 80 eV, 40 eV, 20 eV and 20 eV, respectively. The binding energies were calculated with respect to the C component (BE = 284.8 eV) of the C 1s peak, and a Shirley background subtraction was used. For the spectrum fitting, an XPS analysis program XPS peak 4.1 was used, and a Lorentz–Gauss algorithm was applied. The fitted peak positions were compared with those reported in the literature and the full width half maximum (FWHM) of all the peaks was also used to evaluate the reasonableness of the fitting results. The diffuse reflection spectra were measured with a Shimadzu UV-2700 UV-VIS-NIR spectrometer. A 365 nm LED (ThorLabs) was used as the excitation source for the photoluminescence spectra (PL), persistent luminescence (spectra and decays) and thermoluminescence. For the photoluminescence excitation (PLE), and persistent luminescence excitation spectra, the excitation was provided by an intense Xe plasma

lamp (EQ-99X LDLS, Energetiq Inc.) coupled to a monochromator. For the persistent luminescence excitation measurements, the sample was placed in a fixed sample holder, and the afterglow spectrum was recorded 30 seconds after a 2 minute excitation. The sample was then heated at 300 °C for 5 minutes to thermally empty the traps, then the excitation wavelength was changed and the process reiterated. All the optical measurements above were recorded using a charge coupled device (CCD) camera (Roper Pixis 100) coupled to a visible 300 grooves per mm monochromator (Acton Spectra Pro, Princeton Instruments). The persistent luminescence decay comparison of all studied samples was recorded using a photon-counting device (Optima, Biospace Lab). The samples were arranged in a circle and excited simultaneously using LEDs.

3.Results and discussion

3.1 Crystal structure characterization

$ZnGa_2O_4$ has a normal spinel structure, as shown in **Figure 1**. Normal spinel structures usually belong to the cubic lattice system with two tetrahedral and four octahedral sites per formula unit. Even though there are about 3% antisite defects in the normal spinel lattice of $ZnGa_2O_4$,[9] this situation evolves dramatically with cationic substitution. Indeed, **Figure 1b** shows that Zn^{2+} ions occupy the tetrahedral sites and Ga^{3+} ions occupy the octahedral sites, while Zn_2SnO_4 possesses an inverse spinel structure, where Zn^{2+} ions occupy two different positions: half of these Zn^{2+} ions occupy tetrahedral sites as in normal spinel structure, and the rest occupy the octahedral sites (along with the Sn^{4+} ions). Both of these two materials are cubic close-packed oxides with space group *Fd*-3*m*. In the complex spinel combined by $ZnGa_2O_4$ and Zn_2SnO_4, the tetrahedral sites are expected to be filled by Zn^{2+} ions, the octahedral sites are filled by the rest of the Zn^{2+} ions and all of the Sn^{4+} ions and Ga^{3+} ions. It should be noted that site inversions are expected to be more abundant in this complex spinel than in the pure normal spinel $ZnGa_2O_4$[9].

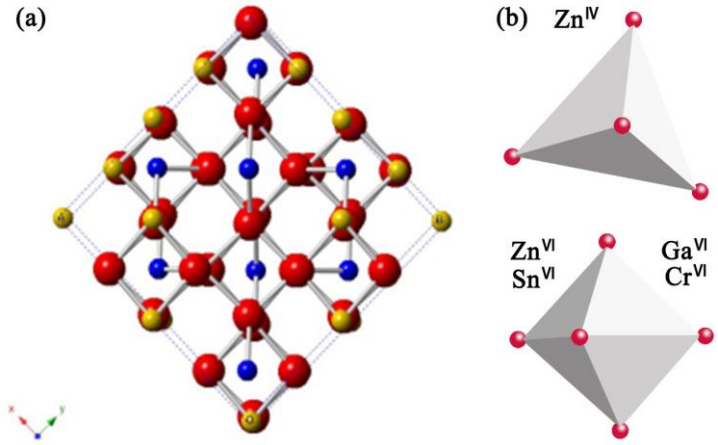

Figure 1. (a) The crystal structure of the normal spinel $ZnGa_2O_4$. The blue spheres represent Zn, red spheres represent O, and yellow spheres represent Ga. (b) Polyhedral view of a complex spinel. The tetrahedral sites are expected to be filled by Zn^{2+} ions, the octahedral sites are filled by the rest Zn^{2+} ions and all the Sn^{4+} ions and Ga^{3+} ions.

A series of Cr^{3+} doped long afterglow materials with a complex spinel (ZGSO) structure were synthesized by the systematic variation of molar ratios between $ZnGa_2O_4$ and Zn_2SnO_4 end members. These samples form a solid solution whose diffraction patterns are consistent with the standard pattern of $ZnGa_2O_4$ (PDF No.086-0413), as shown in **Figure 2**. All of the samples are phase-pure, indicating that complex spinel structures can be obtained through this solid solution approach which combines the normal and inversed spinel structures. In addition, the diffraction peaks of the samples are very sharp and intense, confirming a high degree of crystallinity. As shown in **Figure 2**, with the decrease of the $ZnGa_2O_4$ content, the diffraction peaks of ZGSO shift to a lower angle and become gradually closer to the diffraction peaks of Zn_2SnO_4 (PDF No.074-2184), indicating that the unit cell volumes of the samples are between that of the $ZnGa_2O_4$ and Zn_2SnO_4 spinels. This phenomenon can be explained with Bragg's equation,

$$2d\sin\theta = n\lambda,\ n = 1, 2, 3... \quad (1)$$

where λ is the Cu K_α X-ray wavelength (λ = 0.154178 nm), d is the distance between the two crystal planes and θ is diffraction angle. As shown in **Figure 1**, in the

complex spinel $Zn_{1+x}Ga_{2-2x}Sn_xO_4:Cr^{3+}$, the tetrahedral sites are filled by divalent Zn^{2+} cations, and the octahedral sites are occupied by the remaining Zn^{2+} cations and all of the tetravalent Sn^{4+} and trivalent Ga^{3+} cations. In other words, the complex spinel could be viewed as the substitution of $2Ga^{3+}$ by a Zn^{2+}-Sn^{4+} cation pair. Because the sum of the ionic radii of two Ga^{3+} cations (0.76 Å, CN = VI) is less than the sum of Zn^{2+} (0.88 Å, CN = VI) and Sn^{4+} (0.83 Å, CN = VI)[23], the cell volume of the complex spinel ZGSO and Zn_2SnO_4 are larger than those of $ZnGa_2O_4$. Hence, the *d* value increases, which results in diffraction peaks shifted to a lower angle. Additionally, the XRD results also demonstrate that Cr^{3+} has been doped into ZGSO without changing the crystal structure. Considering that the radius of Cr^{3+} (0.755 Å) is close to that of Ga^{3+} (0.76 Å), Cr^{3+} is inclined to occupy the octahedral Ga^{3+} sites.

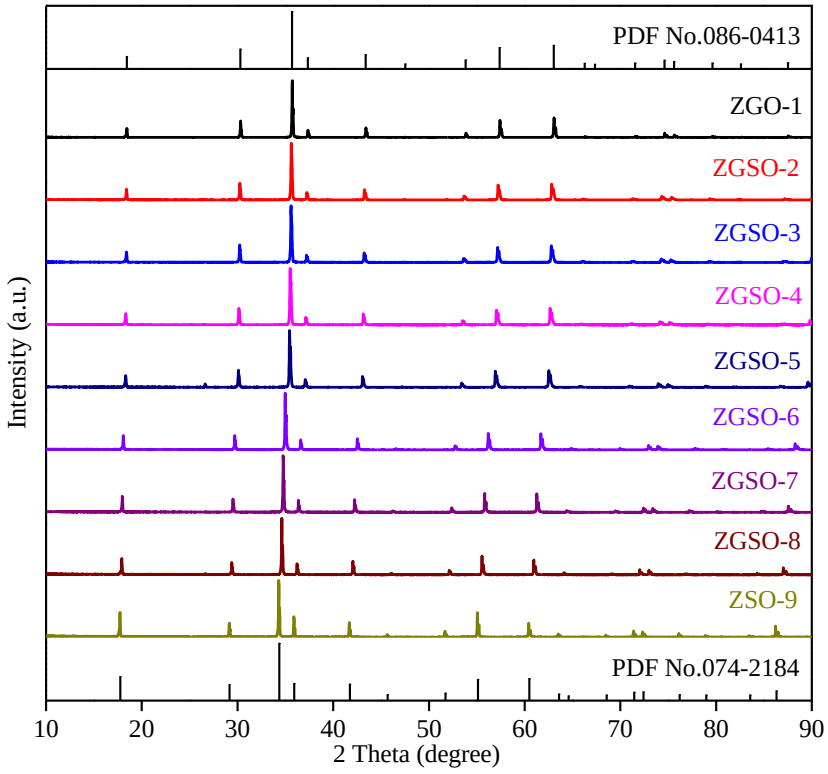

Figure 2. XRD patterns of complex spinel ZGSO, the standard data for $ZnGa_2O_4$ (PDF No.086-0413) and Zn_2SnO_4 (PDF No.074-2184).

XPS studies of the complex spinel ZGSO-3 ($Zn_{10}Ga_{15.92}SnO_{36}$:$0.08Cr^{3+}$) and the ZGO-1 ($ZnGa_2O_4$:$Cr^{3+}$) samples were carried out to confirm the coordination site occupancies of each cation. **Figure 3A** shows the XPS survey scan of ZGO-1 and the

high resolution spectra of Zn 2p, O 1s, Zn LMM and Ga 3d; **Figure 3B** shows the XPS survey scan of ZGSO-3. In **Figure 3(a1)**, the binding energies of 1021.4 eV and 1044.5 eV for Zn 2p peaks can be attributed to the $2p_{3/2}$ and $2p_{1/2}$ states of Zn^{2+} in tetrahedral coordination, respectively. Comparing with **Figure 3(a1)**, the binding energies of Zn 2p in **Figure 3(b1)** are 1021.2 eV and 1044.3 eV, which show no obvious shift. However, the Zn $2p_{3/2}$ peak of ZGSO-3 is broader and can be fitted with two peaks (1021.2 eV and 1023.4 eV), indicating that Zn occupies two sites, *i.e.* the tetrahedral and the octahedral sites, in ZGSO-3. Since higher coordination number will result in higher binding energy, the highest binding energy shoulder should originate from Zn in the six coordinate octahedral sites[24]. The area of the peak with the higher binding energy is smaller than that of the peak with low binding energy, suggesting that the number of Zn atoms in the six coordinate octahedrons is smaller, which is consistent with our design principle. **Figure 3(a3) and (b3)** show the Auger lines of Zn in the ZGO-1 and ZGSO-3 samples. **Figure 3(a2)** shows the high resolution spectra of O 1s of ZGO-1, which can be fitted as three peaks. The highest binding energy originates from the adsorbed oxygen, and the other peaks correspond to the two chemical states of O. As Zn has weaker electronegativity and stronger metallicity than Ga, the lower binding energy is related to the Zn-O bond and the higher binding energy is related to the Ga-O bond.[24] **Figure 3(b2)** shows the high resolution O 1s spectra of ZGSO-3, which can be fitted as four peaks. In comparison with **Figure 3(a2)**, there are additional peaks caused by Sn in the host. Due to the higher electronegativity of Sn compared to those of Ga and Zn, the highest binding energy is related to the Sn-O bond. The high resolution Ga 3d spectra, which overlap with O 2s and Sn 4d, are shown in **Figures 3(a4) and (b4)** respectively. The binding energy of Ga 3d in ZGSO-3 (19.5 eV) appears to be lower than that of Ga 3d in ZGO-1 (20.0 eV). This could be due to the accommodation of Sn in the octahedral sites and the higher electron cloud density for the octahedral Ga environment. **Figure 3(b3)** shows the high resolution Sn 3d and Zn Auger spectra, which can be fitted by

Zn LMM peaks and two Sn 3d peaks, with Sn $3d_{3/2}$ at high binding energy (494.5 eV) and Sn $3d_{5/2}$ at low binding energy (486.0 eV).

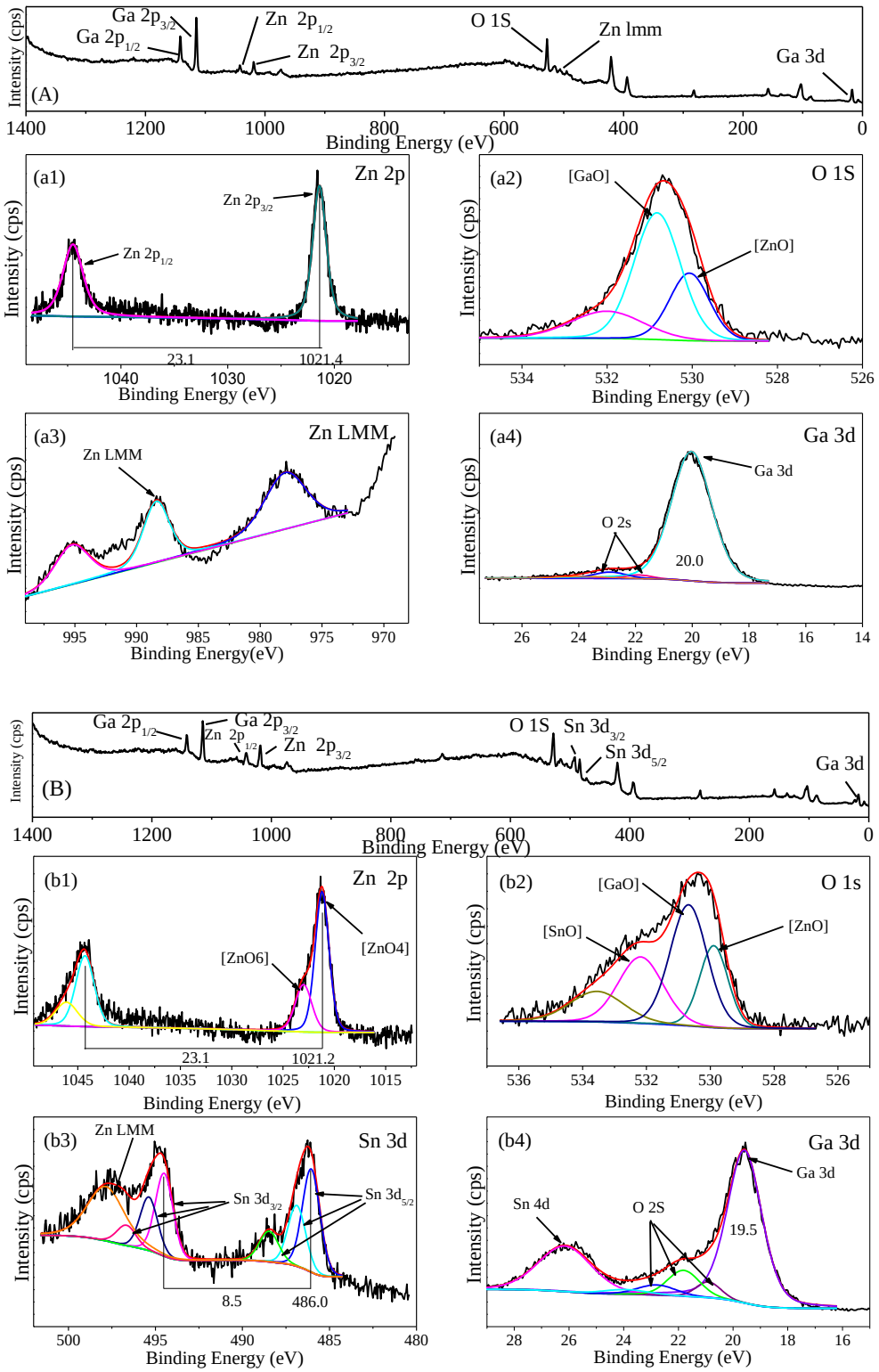

Figure 3. (A) XPS survey scan and high-resolution Zn 2p, O 1s, Zn LMM and Ga 3d XPS spectra of $ZnGa_2O_4$, (B) XPS survey scan and high-resolution Zn 2p, O 1s, Ga 3d and Sn 3d XPS spectra

of ZGSO-3.

Figure 4 shows the high resolution transmission electron microscopy data obtained from a sample of ZGSO-3. As shown in **Figure 4(a)**, the sample exhibits clear lattice fringes, confirming the high degree of crystallinity observed by PXRD. The main d-spacings were measured as 0.295 nm and 0.191 nm, which corresponds to the (220) and (331) Miller planes respectively, as obtained by PXRD. The SAED pattern shows sharp, intense diffraction spots, that can be indexed to the (220), $(13\bar{1})$ and $(\bar{1}3\bar{1})$ reflections of the spinel structure in perfect agreement with the XRD results. By using the high angle annular dark field image probe (HAADF), element distribution mapping of ZGSO-3 was conducted and is shown in **Figure 4(c)**. From the figure, a uniform distribution of the Zn, Ga, Sn, Cr elements and O was observed, demonstrating that the samples are highly homogeneous.

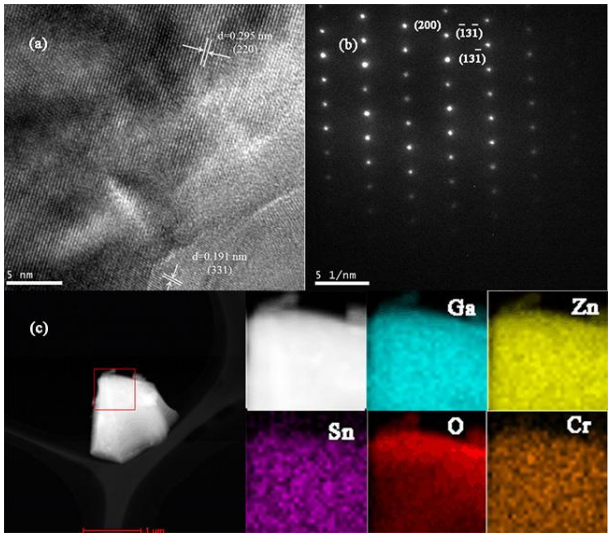

Figure 4. (a) HRTEM images, (b) SAED image, and (c) element distribution mapping of ZGSO-3.

3.2 Diffuse reflectance spectra and photoluminescence properties

Figure 5(a) shows the diffuse reflectance spectra of the complex spinels $Zn_{1+x}Ga_{2-2x}Sn_xO_4:Cr^{3+}$, normal spinel $ZnGa_2O_4:Cr^{3+}$ and inverse spinel $Zn_2SnO_4:Cr^{3+}$. The spectra of all samples show two obvious absorption peaks, peaking for instance for the $ZnGa_2O_4:Cr^{3+}$ sample at 550 nm and 420 nm, which originate from the $^4A_2(^4F) \rightarrow {}^4T_2(^4F)$ and $^4A_2(^4F) \rightarrow {}^4T_1(^4F)$ transitions of Cr^{3+} respectively. The observed

shoulders at around 300 nm are due to the $^4A_2(^4F)\rightarrow{}^4T_1(^4P)$ spin-allowed absorption peak of Cr^{3+}, partially overlapping the band gap edge of $ZnGa_2O_4$. The band gap absorption edge originates from the O^{2-}-Ga^{3+} charge-transfer transition in the $ZnGa_2O_4$ host.[25] With the decrease of the $ZnGa_2O_4$ content, the three absorption peaks of Cr^{3+} shift towards longer wavelengths, due to an increase of the crystal field splitting as the Sn content increases. The band gap absorption edge also shifts gradually towards the longer wavelength, indicating that the band gap becomes smaller when increasing the Zn_2SnO_4 content.

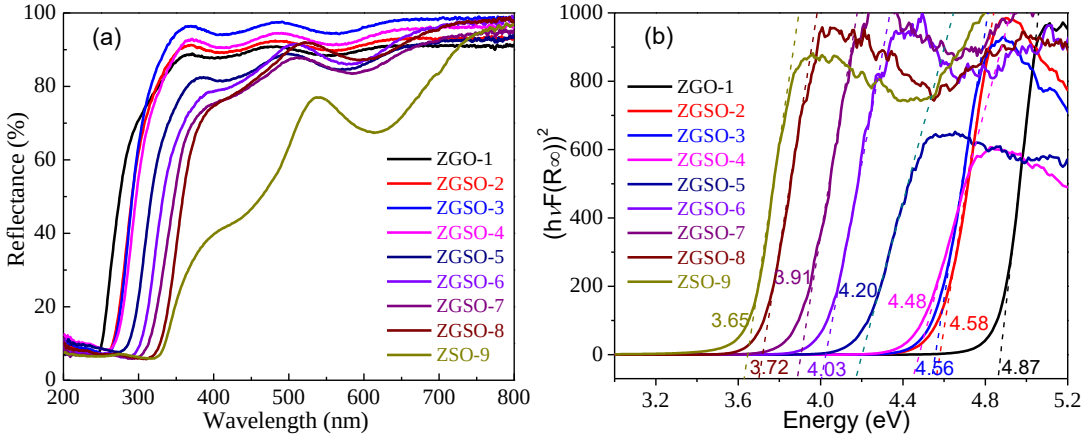

Figure 5. (a) The diffuse reflectance spectra and (b) $(h\upsilon F(R_\infty))^2$-$h\upsilon$ plots of ZGSO-X, ZGO-1 and ZSO-9. The band-gap energy for each sample was estimated from the intercept of the fitted dashed line with $(h\upsilon F(R_\infty))^2 = 0$.

In order to calculate the band gap energies and their variations for all the samples, we convert the diffuse reflectance R_∞ into a Kubelka-Munk function $F(R_\infty)$ as follows:[26]

$$F\left(R_\infty\right)=\left(1-R_\infty\right)^2/2R_\infty \qquad (2)$$

Then one plot $(h\upsilon F(R_\infty))^2$ with $h\upsilon$ according to the equation proposed by Tauc:[27]

$$\left(h\upsilon\times F\left(R_\infty\right)\right)^2=A\times\left(h\upsilon-E_g\right) \qquad (3)$$

where $h\upsilon$ is the photon energy, A represents a proportionality constant and Eg is the band gap energy value. The band-gap energy values can be estimated from the intercepts of fitted straight lines with the $(h\upsilon F(R_\infty))^2 = 0$ horizontal line in the obtained graph, as shown in **Figure 5(b)**. It is found that the band-gap energy values of the

samples decrease gradually from 4.87 to 3.65 eV with increasing Zn_2SnO_4 content. The measured band-gap energy of the $ZnGa_2O_4$ sample in this work is smaller than that reported for samples prepared via hydrothermal methods (5.07 eV), but larger than that reported for samples prepared by solid state methods (4.76 eV).[28] The latter tends to be smaller due to a Zn deficiency induced at high sintering temperatures [7]. The value of the band gap of pure Zn_2SnO_4 agrees well with the one reported previously.[17]

Figure 6(a) presents the photoluminescence excitation (PLE) spectra of ZGSO, ZGO-1 and ZSO-9, monitoring their emission at 696 nm. The PLE spectra of all samples possess a strong band-to-band absorption and three excitation bands due to the $^4A_2(^4F)\rightarrow{}^4T_2(^4F)$, $^4A_2(^4F)\rightarrow{}^4T_1(^4F)$ and $^4A_2(^4F)\rightarrow{}^4T_1(^4P)$ transitions of Cr^{3+}, which are in agreement with the absorption bands in the diffuse reflectance spectra. Taking the PLE spectrum of ZGSO3 as an example, it contains a strong and broad excitation band located at 272 nm, which can be attributed to the VB→CB transition of the host. The other peaks at 555 nm, 404 nm and the shoulder at 320 nm can be assigned as $^4A_2(^4F)\rightarrow{}^4T_2(^4F)$, $^4A_2(^4F)\rightarrow{}^4T_1(^4F)$ and $^4A_2(^4F)\rightarrow{}^4T_1(^4P)$ transitions of Cr^{3+} respectively.[17,29] The VB→CB absorption feature is slightly red shifted from 274 nm to 292 nm and its intensity decreases with the increase of the inverse spinel Zn_2SnO_4 content. As shown in **Figure 6(b)** and **Table 2**, with the increase of the inverse spinel Zn_2SnO_4 content, the $^4A_2(^4F)\rightarrow{}^4T_2(^4F)$ band shifts towards the red range (*i.e.* 550 nm for $ZnGa_2O_4$:Cr^{3+} and 598 nm for Zn_2SnO_4:Cr^{3+}) with declining intensity. This is related to the decreasing crystal field strength of the solid solution as the proportion of inverse spinel increases. Hence, the energy levels of $^4T_2(^4F)$, $^4T_1(^4F)$ and $^4T_1(^4P)$ manifolds shift downwards, as presented in the d^3 Tanabe-Sugano diagram presented **Figure 7**. For a more quantitative analysis, the crystal field strength *Dq* and the Racah parameters *B* can be estimated by the energy of various excitation peaks as follows :[30]

$$10D_q = \upsilon_2 \qquad (4)$$

$$B = \left(\upsilon_1^2 + \upsilon_2^2 - 3\upsilon_1\upsilon_2\right) \Big/ \left(15\upsilon_1 - 27\upsilon_2\right) \qquad (5)$$

where v_1 and v_2 are the energy corresponding to Cr^{3+} ions [$^4A_2 \rightarrow {}^4T_1$] and [$^4A_2 \rightarrow {}^4T_2$] transitions, respectively. The obtained results are presented in **Table 2** and marked in **Figure 7** with vertical lines.

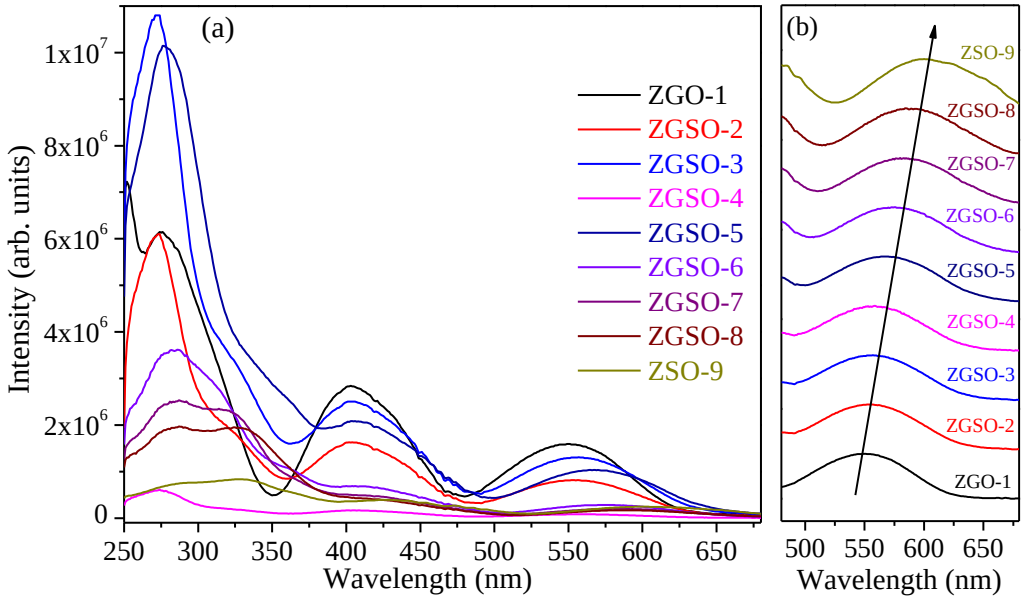

Figure 6. (a) PLE spectra of all ZGSO samples, including ZGO-1 and ZSO-9. (b) The normalized PLE spectra ranging from 480 to 680 nm for all samples.

Table 2. Peak position of PLE and estimated crystal field parameters of Cr^{3+} in the complex spinel samples ZGSO, ZGO-1 and ZSO-9.

	$^4A_2 \rightarrow {}^4T_1$ [nm]	$^4A_2 \rightarrow {}^4T_2$ [nm]	Dq [cm^{-1}]	B [cm^{-1}]	Dq/B
ZGO-1	403	550	1818	645	2.818
ZGSO-2	404	553	1808	651	2.778
ZGSO-3	405	557	1795	661	2.717
ZGSO-4	406	558	1792	657	2.726
ZGSO-5	410	568	1761	670	2.626
ZGSO-6	412	575	1739	686	2.537
ZGSO-7	417	580	1724	669	2.577
ZGSO-8	421	589	1698	677	2.508
ZSO-9	425	598	1672	685	2.442

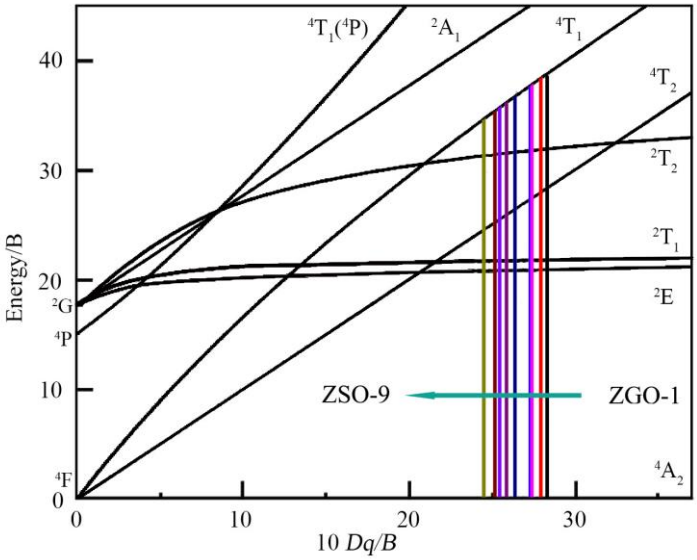

Figure 7. Tanabe-Sugano diagram of Cr^{3+} with d^3 electron configuration in the complex spinel samples ZGSO-X, ZGO-1 and ZSO-9.

Photoluminescence (PL):

In the previous section, we highlighted the evolution of the excited states energies (via the Tanabe-Sugano diagram) as a function of the compositional variation. In the following section, the evolution of the emission properties is presented. The normalized PL spectra are shown in **Figure 8**. For the $ZnGa_2O_4:Cr^{3+}$ (ZGO-1) reference compound, the expected Cr^{3+} $^2E \rightarrow {}^4A_2$ PL spectrum is observed, and is composed of several sharp lines including the R1, R2, N1 and N2 lines, which are well reported and characteristic of chromium on the gallium octahedral site.[31,32] When Sn^{4+} substitutes for Ga^{3+}, several modifications of the PL spectra are observed. Initially, the Cr^{3+} emission lines broaden with increasing Sn^{4+} content. This can be explained by the increased Cr^{3+} nearest-neighbor disorder as the Sn^{4+} content increases. In parallel, a large contribution appears in the deep red range between 700 nm and 900 nm and shifts towards higher wavelengths as the Sn^{4+} content continues to increase. This broad band can be attributed to the Cr^{3+} $^4T_2 \rightarrow {}^4A_2$ emission as already reported in the literature for the zinc gallate host.[33] Furthermore, the

observed redshift is in good agreement with the crystal field evolution as determined by the excitation spectra.

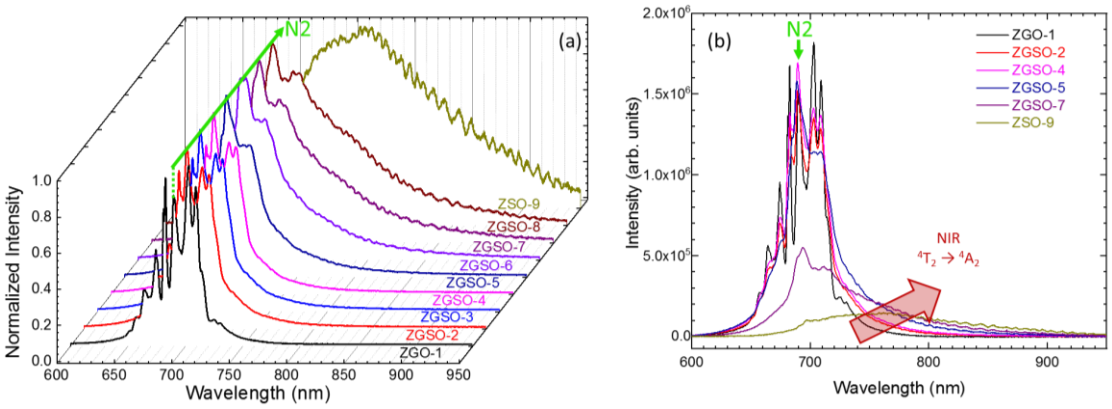

Figure 8: (a) Normalized PL spectra of the ZGO-1, ZGSO-X and ZSO-9 samples. (b) PL emission spectra of the samples with highlighted N2 line and $^4T_2 \rightarrow {}^4A_2$ emission band. For all measurements, a 365 nm LED was used as excitation source.

Persistent luminescence:

In the previous paragraph, we demonstrated that the increase of the Sn^{4+} content leads to a significant red shift of the Cr^{3+} $^4T_2 \rightarrow {}^4A_2$ emission. The purpose of the following part is to study what occurs to the persistent luminescence alongside the solid solution. The normalized persistent luminescence (AG-PL) spectra are presented in Figure 9 (a). As soon as Sn^{4+} substitutes for Ga^{3+}, the predominance of N2 increases and the R lines become barely distinguishable. In addition, the broad band contribution of the Cr^{3+} $^4T_2 \rightarrow {}^4A_2$ on the persistent luminescence spectra increases and shifts towards the near infrared range as the Sn^{4+} content increases. However, the signal to noise ratio suggests that the persistent luminescence intensity of ZGSO-7, ZGSO-8 and ZSO-9 is lower compared to compounds with less Sn^{4+} substitution. The persistent luminescence decay profiles, presented in Figure 9 (b) confirm that at some point, the increase of Sn^{4+} content lowers the persistent luminescence intensity. Still, it can be observed that low Sn^{4+} content compounds (ZGSO-2, ZGSO-3 and ZGSO-4) possess persistent luminescence intensities comparable and even better to the ZGO-1 reference material. Indeed, the ZGSO-2 and ZGSO-3 phosphors have higher performance and persistent luminescence intensity than ZGO-1 in the first minutes

after stopping the UV excitation (for instance 55 s for ZGSO-3 and 123 s for ZGSO-2). The higher intensity and faster decay of the persistent emission of tin substituted zinc gallates suggests shallower traps compared to ZGO-1. The trap evolution in these materials will be further studied using thermoluminescence (TL). Nevertheless this behavior should be very interesting for bioimaging applications.

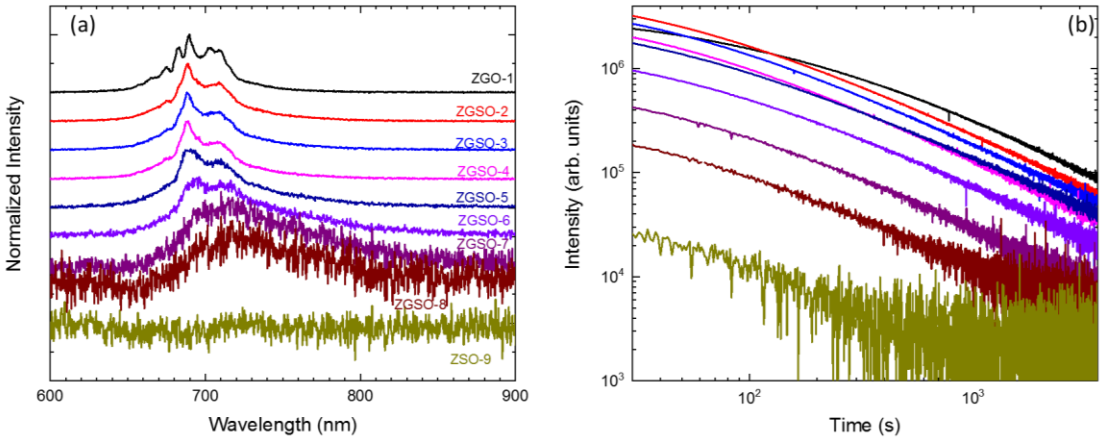

Figure 9: (a) Normalized persistent luminescence spectra of ZGO-1, ZGSO-X and ZSO-9 samples recorded 1 min after 365 nm excitation for 5 min. (b) Persistent luminescence decays of the same samples using the same excitation conditions.

As demonstrated in Figure 6 (absorption and excitation spectra), both the band-to-band energy and the energies between the $^4A_2$ and the ^4T levels decrease with Sn^{4+} content. In order to find out if the observed redshifts can be useful for charging the persistent luminescence, the persistent luminescence excitation spectra (also called AG-PLE) were recorded (see Figure 10). In this figure, the persistent luminescence excitation spectrum of the reference sample (ZGO-1) is compared to the ZGSO-4 and ZGSO-5 with intermediate dopant content. The ZGO-1 AG-PLE spectrum is composed of one intense band peaking at 320 nm and one weaker band centered around 600 nm. This is consistent with previous results obtained by Bessière *et al*[34] in which the high energy band was associated with the charging through the bandgap with conduction band mixed with the $^4A_2 \rightarrow {}^4T_1$ transition, whereas the low energy band was related to the charging through the $^4A_2 \rightarrow {}^4T_2$ band triggered by a local electric field.[31] The ZGSO-4 and ZGSO-5 AG-PLE spectra are slightly different.

Although the high energy band is lower compared to the ZGO-1 material, an interesting red shift is found as the Sn^{4+} content increases. This redshift is of major importance for persistent luminescence charging using blue LEDs which are less expensive and more powerful compared to UV sources. More interestingly, we observe that the low energy bands are not only shifted towards the deep red range but are also more intense when Sn^{4+} is added. This is of major interest for persistent luminescence materials used for *in vivo* imaging. Indeed, the ZGSO-5 material will be the compound with the highest persistent luminescence intensity with deep red charging, which is an important requirement for *in vivo* charging and long-term bioimaging.[7]

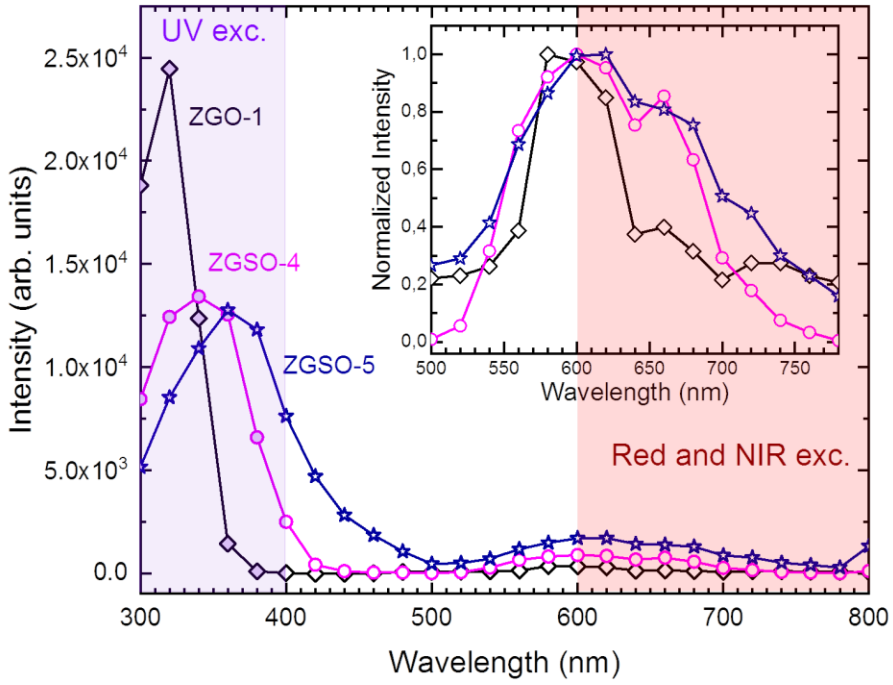

Figure 10: Persistent luminescence excitation spectra of ZGO-1, ZGSO-4 and ZGSO-5 samples.

In order to analyze the persistent luminescence decays (Figure 9) and the persistent luminescence excitation spectra (Figure 10) in more detail, a photon counting imaging

camera was used to record the persistent luminescence intensity after several excitation modes. It is important to note that this system leads to an approximate maximal error of 10%. After 365 nm excitation (Figure 11 (a), (c) and (d)) it is notable that, with the exception of ZGSO-2 (in the 10 % error bar range), the persistent luminescence intensity decreases when Sn^{4+} content increases. Moreover, the difference between integrated intensity after 25 min and 70 min is smaller for ZGO-1 than ZGSO-2 which corresponds to a slower persistent luminescence decay for ZGO-1. These results are in good agreement with the AG-PL and AG-PLE results previously presented. The procedure was repeated with 625 nm excitation (Figure 11 (b), (e) and (f)), an excitation wavelength with smaller energy at the edge of the first biological window where the transparency of the tissue starts to be efficient. It is found that the highest persistent luminescence intensity is obtained for a partially tin substituted compound, ZGSO-5, in good agreement with the AG-PLE measurements. In a same way, the integrated intensity of the persistent luminescence was recorded after exposure to ambient laboratory light *i.e.* visible light charging (see Figure S1). Again, the integrated intensity was found to increase from ZGO-1 to ZGSO-5 and then decreases at higher tin contents, in good agreement with the blue shift of the charging bands observed with AG-PLE results. The integrated intensity difference between 6 min and 17 min after 625 nm excitation is lower for ZGO-1 compared to ZGSO-5. This indicates that the trapping is more efficient for the ZGSO-5 tin partially substituted compound than ZGO-1 but that the trap depth should decrease with increasing tin content.

The following part of the paper is dedicated to the study of the evolution of the trap depths and trap distribution with Sn^{4+} content by means of thermoluminescence.

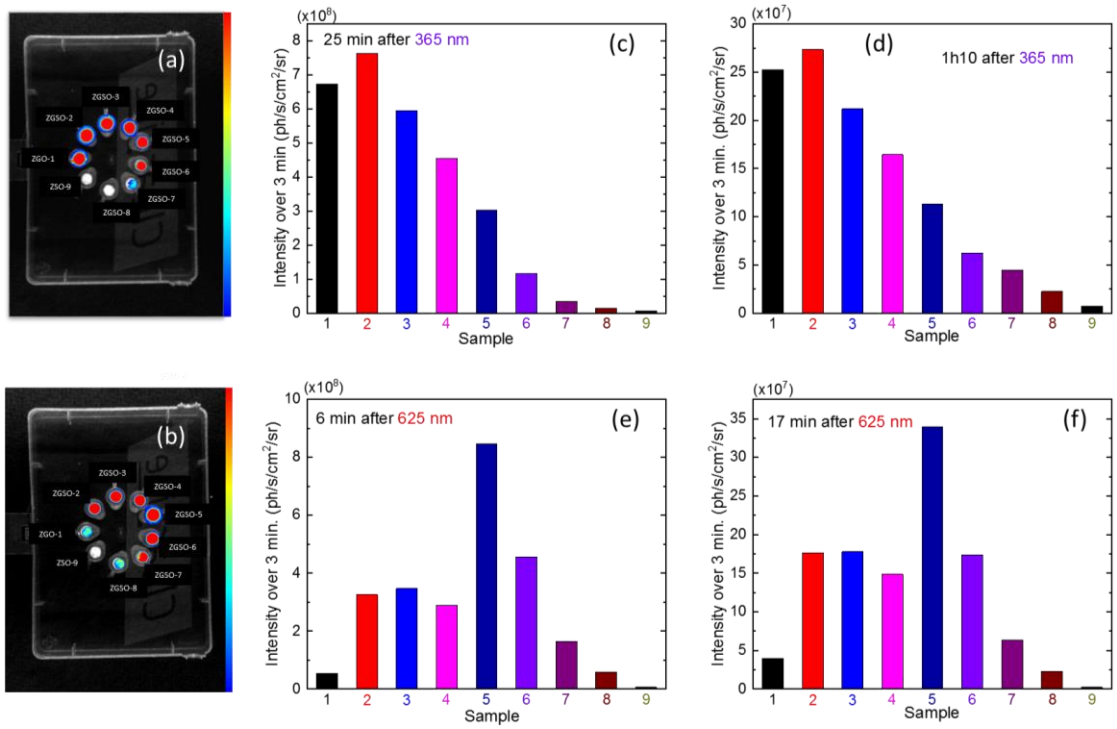

Figure 11: Pictures of the samples using photon counting system (a) 25 min after UV (365 nm) excitation and (b) 6 min after 625 nm excitation. The diagrams represent the persistent luminescence intensity integrated during 3 min (c) 25 min after 365 nm, (d) 70 min after 365 nm, (e) 6 min after 625 nm and (f) 17 min after 625 nm excitation.

To highlight the great potential of ZGSO complex spinels for *in vivo* imaging, the persistent luminescence emission of three selected samples was carried out under a 7 mm thick raw pork slice (Figure 12 (a)). To demonstrate the possible *in vivo* activation of the persistent luminescence, the samples were excited with a 625 nm red LED through the raw pork slice. The samples were previously heated at 300 °C to ensure that no charges were trapped before charging with the red LED. After the red light charging through the raw pork slice, all the samples present persistent luminescence decays as presented on Figure 12 (b) and (c). The number of the persistent photons collected with the camera through the raw pork slice increase drastically from ZGO-1 reference spinel to ZGSO-5. Indeed, the number of photons collected for ZGSO-5 is 400 times higher compared to ZGO-1 reference material 90 s after stopping the excitation. This result is consistent with the increasing persistent luminescence charging using in the deep red range for partially tin substituted samples.

This strong increase of the collected persistent luminescence evidences the tremendous interest of the ZGSO-5 sample for possible *in vivo* bio-imaging.

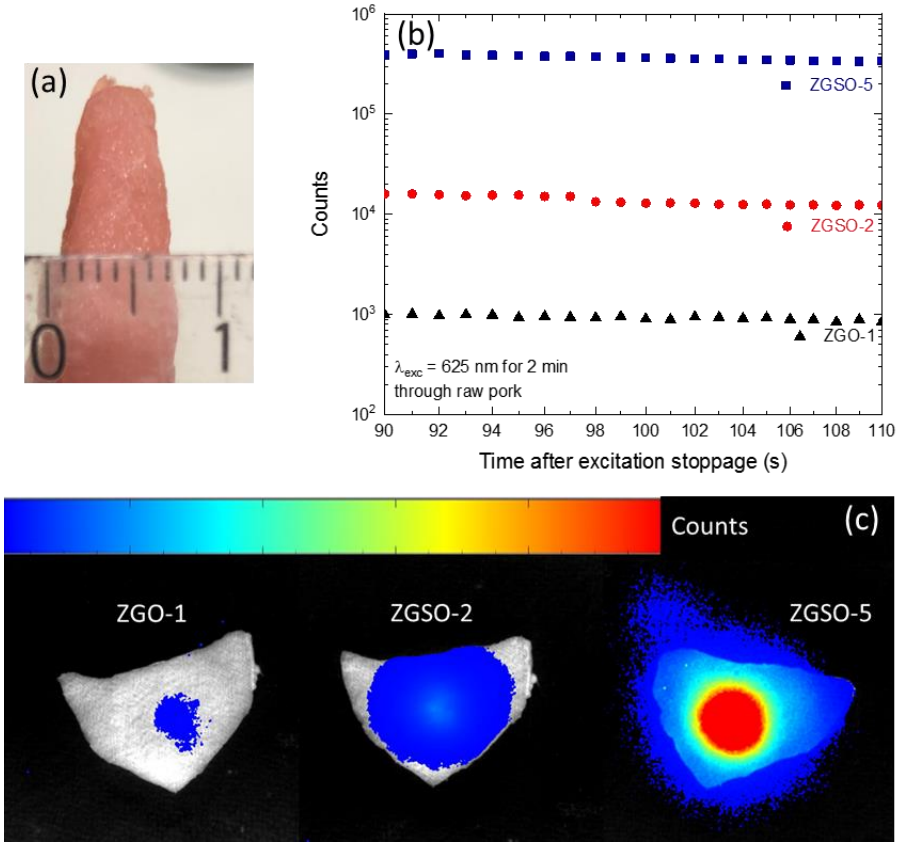

Figure 12: (a) Picture of the raw pork slice used for the measurements. (b) Persistent luminescence decays of ZGO-1 (black triangles), ZGSO-2 (red dots) and ZGSO-5 (blue squares) recorded 90 s after 2 minutes of 625 nm excitation through the raw pork slice. (c) Pictures of the samples under the raw pork slice using the photon counting system.

Thermoluminescence:

The persistent luminescence decay curves of the different compounds have different slopes revealing an evolution of the persistent luminescence kinetics and an evolution of the trap depths. To study the trap positions of each compound, we performed thermoluminescence studies. From the normalized TL profiles (**Figure 13 (a)**), we observe that the trap depths decrease with the increase of Sn^{4+} content. This is

consistent with the steeper slopes of the decay profiles with higher Sn^{4+} contents. Moreover, the TL bands are broader when Sn^{4+} substitutes for Ga^{3+}. This can be related to the increasing number of Sn_{Ga}° and Zn_{Ga}' defects. These two defects can act as electron and hole traps respectively. The TL glow curves (Figure S2) have been integrated to compare the persistent luminescence efficiency and the total trap capability (Figure 13 (b)). In order to compare the persistent luminescence efficiency, the profiles have been integrated between 298 and 313 K, which is the useful temperature range for applications. The persistent luminescence efficiency decreased all along the solid solution. To estimate the total trap capacity, the whole thermoluminescence spectra have been integrated, even in low temperature ranges (where the de-trapping occurs immediately after stopping the excitation) and at high temperature ranges (where at room temperatures the trapped charges cannot be de-trapped). Unlike the persistent luminescence efficiency, a small Sn^{4+} content can improve the total charge trapping and the charging of the materials. This explains why the persistent luminescence profiles of ZGSO-2 and ZGSO-3 are higher than ZGO-1 at short times after stopping the excitation, and validates the interest in studying these compounds.

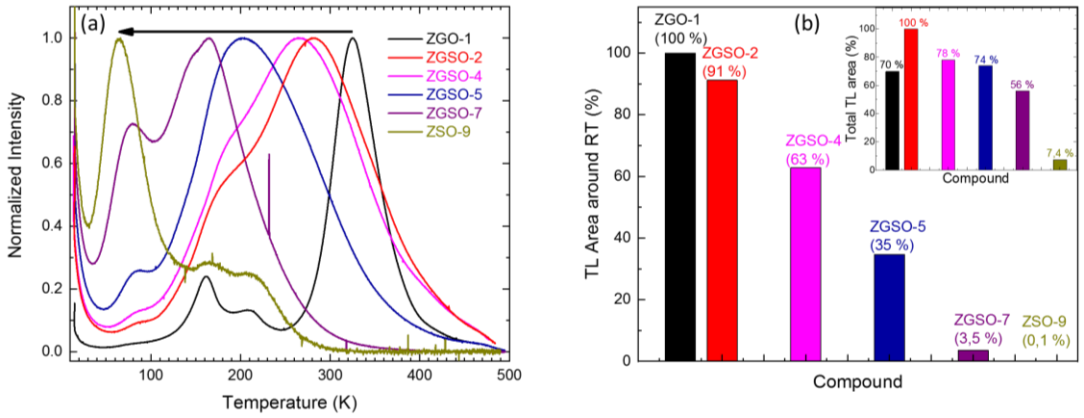

Figure 13: (a) Thermoluminescence glow curves of selected samples after UV excitation during 5 minutes at 14 K. (b) TL integrated intensity around RT relative to ZGO-1, representing the persistent luminescence efficiency at room temperature. Inset, total TL integrated intensity relative to ZGSO-2, representing the total storage capacity of the persistent phosphors.

Discussion:

The optical results obtained from the materials mainly indicate the following evolutions with the tin substitution:

(i) A redshift of the main persistent luminescence excitation band;

(ii) A decrease in intensity of this main persistent luminescence excitation band;

(iii) A redshift of the persistent luminescence excitation band related to chromium bands;

(iv) An intensity increase of this persistent luminescence excitation band;

(v) A shift towards lower temperature of the thermoluminescence bands;

(vi) A broadening of the thermoluminescence bands;

(vii) An decrease intensity of the thermoluminescence signal (around RT)

In the following part we tentatively explain why these properties evolve in this way with the composition, and propose a set of schematic energy-level diagrams (as presented in Figure 14) to illustrate this interpretation.

The decrease of the band gap energy with the increase of Sn^{4+}/Ga^{3+} substitution can explain process (i). Indeed, a decrease of the band gap can lead to a decrease in the energy difference between the Cr^{3+} ground state and the conduction band. This is observed through the shift of the main excitation band. This process is schematized in **Figure 14** by the decreasing length of the dotted arrows and by the color going from violet to blue.

The crystal field strength variation, illustrated in the Tanabe-Sugano diagram, [(see Figure 7)] explains the decrease in the energy difference between the Cr^{3+} $^4A_2$ and $^4T_2$ levels and the redshift of the low energy persistent excitation band [observation (iii)].

The shift towards low temperature of the TL bands (v) may be explained either by the decrease of the bandgap energy or by the decrease of the crystal field as

de-trapping is assumed to occur through the band gap and the chromium excited bands.[31,34]

The decrease in intensity of the persistent excitation band in the UV/blue range (ii) reveals the decreases of the useful traps when persistent luminescence is required. The lowering of the trap depths observed with TL may explain this decrease. In **Figure 14**, the useful and ineffective traps are presented in green and red respectively. This decrease of the relevant traps is consistent with the decrease of the thermoluminescence signal around room temperature (vii), yet the total TL glow curve is higher for ZGSO-2 and ZGSO-4 than for ZGO-1, which indicates a higher total storage capability.

The trapping processes have been linked to the antisite defects stabilized in the local environment of Cr^{3+},[31,35] and ^{71}Ga NMR studies have previously shown that the antisite content first increases and then decreases with Ga^{3+}/Sn^{4+} substitution.[8] These results can explain the first increase of the total storage capability (from ZGO-1 to ZGSO-2) followed by its decrease along the solid solution.

The TL peak broadening (vi) can be linked to the defect distribution, particularly to the antisite defects, which increases with tin content.

Finally, the increasing charging efficiency through the Cr^{3+} bands (iv) is observed from ZGO-1 to ZGSO-5. It could be linked to an increase of the local electric field brought by the antisite defects around Cr^{3+}. The evolution of the surrounding local environment of Cr^{3+} with Sn^{4+} substitution for Ga^{3+} is clearly observed in the EPR spectra (see Figure S3). This evolution is schematized by the yellow “lighting” arrow in Figure 14.

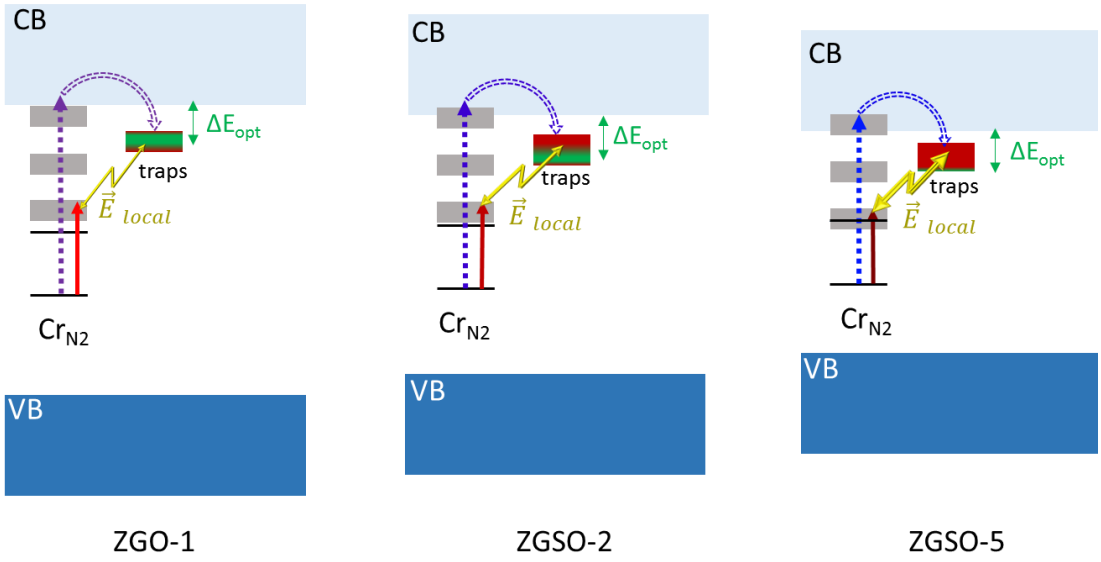

Figure 14: Schematic representation of the energy diagram evolution to model the evolution of the luminescence properties with the material composition. In this scheme, the trapping through the charge transfer from Cr^{3+} to the conduction band is represented by dotted arrows. The decreasing energy required for this process is schematized by the decreasing size and the color shift of the arrows from violet to blue. The trapping through the chromium bands is represented by the red solid arrows and their required energies are schematized by their size and tint. The local electric field that triggers the charging through chromium bands is represented by the yellow "lighting" arrows. Its efficiency is schematized by the arrows thickness. The red part of the traps represents traps that are not involved in the persistent luminescence process (traps that are too deep or too shallow for instance) whereas the green part represents the "useful" part when bioimaging applications are envisioned.

4. Conclusions

Pure spinel phases can be obtained through a solid solution approach to combine the normal and inverse spinel structures. In the complex spinel, the tetrahedral sites are filled by Zn^{2+} divalent cations, and the octahedral sites are occupied by the remaining Zn^{2+} cations together with all the tetravalent Sn^{4+} cations and the trivalent Ga^{3+} cations. Gallium substitution by tin appears as a good strategy to redshift both the large chromium excitation and emission bands, which is due to the variation in crystal field strength. The tin substitution is easily performed and makes only small modifications to the structural and crystalline properties, but has a comparatively large influence on the optical properties. While increasing the tin concentration, the trap depths slightly decrease which increases the persistent luminescence decay rate, but this is associated with a large

increase of the total storage capability. Indeed with tin substitution, compounds have higher total storage capacity compared to $ZnGa_2O_4:Cr^{3+}$.

Since persistent emission is redshifted into the deep red region, this could be a useful way to tune the emission in the biological window and manage diffusion problems. More interestingly, persistent luminescence excitation bands are also redshifted and strongly enhanced in the blue and orange/red ranges. Therefore, the activation of persistent luminescence toward the visible range instead of the UV range is much easier for the $Zn_{1.33}Ga_{1.34}Sn_{0.33}O_4:Cr^{3+}$ compared to $ZnGa_2O_4:Cr^{3+}$. In addition to this redshift, the low energy charging band also appears more intense for $Zn_{1.33}Ga_{1.34}Sn_{0.33}O_4:Cr^{3+}$ compared to $ZnGa_2O_4:Cr^{3+}$. This is of major interest for the further development of persistent luminescence materials suitable for *in vivo* imaging as their re-activation through the living tissues will be more efficient.

Acknowledgments

This work was supported by the National Natural Science Foundation of China (Project No. 10804099, 21804119), Key projects of Zhejiang Natural Science Foundation (Project No. LZ18B050002).

Received: ((will be filled in by the editorial staff))
Revised: ((will be filled in by the editorial staff))
Published online: ((will be filled in by the editorial staff))

References

(1) Wu, S. L.; Pan, Z. F.; Chen, R. F.; Liu, X. G. Long Afterglow Phosphorescent Material. *Springer International Publishing AG*, Switzerland **2017.**

(2) Li, Y.; Gecevicius, M.; Qiu, J. Long Persistent Phosphors—from Fundamentals to Applications. *Chem. Soc. Rev.* **2016**, *45*, 2090.

(3) Lécuyer, T.; Teston, E.; Ramirez-Garcia, G.; Maldiney, T.; Viana, B.; Seguin, J.; Mignet, N.; Scherman, D.; Richard, C. Chemically Engineered Persistent Luminescence Nanoprobes for Bioimaging. *Theranostics* **2016**, *6*, 2488-2523.

(4) Liu, J.; Lécuyer, T.; Seguin, J.; Mignet, N.; Scherman, D.; Viana, B. Imaging and Therapeutic Applications of Persistent Luminescence Nanomaterials. *Adv. Drug. Deliv. Rev.* **2019**, *138*, 193-210.

(5) Frangioni, J. V. *In vivo* Near-infrared Fluorescence Imaging. *Current Opinion in Chemical Biology.* **2003**, *7*, 626-634.

(6) Chermont, Q. L. M. D.; Chanéac, C.; Seguin, J.; Pellé, F.; Maîtrejean, S.; Jolivet, J. -P.; Gourier, D.; Bessodes, M.; Scherman, D. Nanoprobes with Near-Infrared Persistent Luminescence for *in vivo* Imaging. *Proc. Natl. Acad. Sci. U. S. A.* **2007**, *104*, 9266-9271.

(7) Bessière, A.; Jacquart, S.; Priolkar, K.; Lecointre, A.; Viana, B.; Gourier, D. $ZnGa_2O_4:Cr^{3+}$: a New Red Long-lasting Phosphor with High Brightness. *Opt. Express* **2011**, *19*, 10131-10137.

(8) Maldiney, T.; Bessière, A.; Seguin, J.; Teston, E.; Sharma, S. K.; Viana, B.; Bos, Dorenbos, A. J. J.; P.; Bessodes, M.; Gourier, D.; Scherman, D.; Richard, C. The *in vivo* Activation of Persistent Nanophosphors for Optical Imaging of Vascularization, Tumours and Grafted Cells. *Nat. Mater.* **2014**, *13*, 418-426.

(9) Allix, M.; Chenu, S.; Véron, E.; Poumeyrol, T.; Kouadri-boudjelthia, E. A.; Alahraché, S.; Porcher, F.; Massiot, D.; Fayon, F. Considerable Improvement of Long-Persistent Luminescence in Germanium and Tin Substituted $ZnGa_2O_4$. *Chem. Mater.* **2013**, *25*, 1600-1606.

(10) Abdukayum, A.; Chen, J.; Zhao, Q.; Yan, X. Functional Near Infrared-Emitting Cr^{3+}/Pr^{3+} Co-Doped Zinc Gallogermanate Persistent Luminescent Nanoparticles with Superlong Afterglow for *in vivo* Targeted Bioimaging. *J. Am. Chem. Soc.* **2013**, *135*, 14125-14133.

(11) Liu, F.; Chen, Y.; Liang, Y.; Pan, Z. Phonon-Assisted Upconversion Charging in $Zn_3Ga_2GeO_8:Cr^{3+}$ Near-Infrared Persistent Phosphor. *Opt. Lett.* **2016**, *41*, 954-957.

(12) Zhao, H.; Yang, C.; Yan, X. Fabrication and bioconjugation of B^{III} and Cr^{III} Co-doped $ZnGa_2O_4$ Persistent Luminescent Nanoparticles for Dual-Targeted Cancer Bioimaging. *Nanoscale* **2016**, *8*, 18987-18994.

(13) Castaing, V.; Sontakke, A. D.; Xu, J.; Fernández-Carrión, A. J.; Genevois, C.; Tanabe, S.; Allix, M.; Viana, B. Persistent Energy Transfer in ZGO:Cr^{3+} ,Yb^{3+}: A New Strategy to Design Nano Glass-Ceramics Featuring Deep Red and Near Infrared Persistent Luminescence. *Phys. Chem. Chem. Phys.* **2019**, *21*, 19458-19468.

(14) Zhuang, Y.; Ueda, J.; Tanabe, S. Enhancement of Red Persistent Luminescence in Cr^{3+}-Doped $ZnGa_2O_4$ Phosphors by Bi_2O_3 Codoping. *Applied Physics Express* **2013**, *6*, 2602.

(15) Pan, Z.; Lu, Y.; Liu, F. Sunlight-activated Long-Persistent Luminescence in the Near-Infrared from Cr^{3+}-Doped Zinc Gallogermanates. *Nat. Mater.* **2011**, *11*, 58-63.

(16) Shen, F.; Deng, C.; Wang, X.; Zhang, C. Effect of Cr on Long-Persistent Luminescence of Near-Infrared Phosphor $Zn_3Ga_2Ge_2O_{10}$:Cr^{3+}. *Mater. Lett.* **2016**, *178*, 185-189.

(17) Li,Y.; Li, Y.; Sharafudeen, K.; Dong, G.; Zhou, S.; Ma, Z.; Peng, M.; Qiu, J. Long Persistent and Photo-Stimulated Luminescence in Cr^{3+}-Doped Zn-Ga-Sn-O Phosphors for Deep and Reproducible Tissue Imaging. *J. Mater. Chem. C* **2014**, *2*, 2637-2816.

(18) Li, Y.; Li, Y.; Chen, R.; Sharafudeen, K.; Zhou, S.; Gecevicius, M.;Wang, H.; Dong, G.; Wu, Y.; Qin, X.; Qiu, J. Tailoring of the Trap Distribution and Crystal Field in Cr^{3+}-Doped non-gallate Phosphors with Near-Infrared Long-Persistence Phosphorescence. *Npg Asia Mater*. **2015**, *7*, e180.

(19) Sickafus, K. E.; Wills, J. M.; Grimes, N. W. Structure of Spinel. *J. Am. Chem. Soc.* **1999**, *82*, 3279-3292.

(20) Zerarga, F.; Bouhemadou, A.; Khenata, R.; Bin-Omran, S. Structural, Electronic and Optical Properties of Spinel Oxides $ZnAl_2O_4$, $ZnGa_2O_4$ and $ZnIn_2O_4$. *Solid State Sci.* **2011**, *42*, 1638-1648.

(21) Cogle, T. J.; Mateus, C. A. S.; Binks, J. H.; Irvine, J. T. S. Solid-Solution Formation, Electrical Properties and Zero-Resistance Behaviour in the Spinel System Mg_2TiO_4-$MgTi_2O_4$. *J. Mater. Chem.* **1991**, *1*, 289-291.

(22) Sun, X.; Wang, S.; Shen, C.; Xu, X. Efficient Photocatalytic Hydrogen Production over Rh-Doped Inverse Spinel Zn_2TiO_4. *Chemcatchem* **2016**, *8*, 2289-2295.

(23) Shannon, R. D.; Prewitt, C. T. Effective Ionic Radii in Oxides and Fluorides. *Acta Crystallographica. Section B, Structural Science* **1969**, *25*, 925-946.

(24) Briggs, D. Handbook of X-ray Photoelectron Spectroscopy, ed.C. D. Wanger, W. M. Riggs, L. E. Davis, J. F. Moulder and G. E. Muilenberg, Perkin-Elmer Corp., Physical Electronics Division, Eden Prairie, Minnesota, USA, 1979, pp. 190. *Surf. Interface Anal*. **1981**, *3.*

(25) Sharma, S. K.; Bessière, A.; Basavaraju, N.; Priolkar, K. R.; Binet, L.; Viana, B.; Gourier, D. Interplay between Chromium Content and Lattice Disorder on Persistent Luminescence of $ZnGa_2O_4$:Cr^{3+} for *in vivo* Imaging. *J. Lumin.* **2014**, *155*, 251-256.

(26) Džimbeg-Malčić, V.; Barbarić-Mikočević, Ž.; Itrić, K. Kubelka-Munk Theory in Describing Optical Properties of Paper (II). *Teh. Vjesn.* **2012**, *19*, 191-196.

(27) Tauc, J. Optical Properties and Electronic Structure of Amorphous Ge and Si. *Materials Research Bulletin* **1968**, *3*, 37-46.

(28) Zhang, Y.; Wu, Z. J.; Geng, D. L.; Kang, X. J.; Shang, M. M.; Li, X. J. Full Color Emission in $ZnGa_2O_4$: Simultaneous Control of the Spherical Morphology, Luminescent, and Electric Properties via Hydrothermal Approach. 6581.*Adv. Funct. Mater.* **2014**, *24*, 6581-6593.

(29) Brito, H. F.; Hölsä, J.; Jungner, H.; Laamanen, T.; Lastusaari, M.; Malkamaki, M.; Rodrigues, L. C. V. Persistent Luminescence Mechanisms: Human Imagination at Work. *Opt. Mater. Express* **2012**, *2*, 371-381.

(30) Chen, D.; Chen, Y.; Lu, H.; Ji, Z.; A Bifunctional Cr/Yb/Tm:$Ca_3Ga_2Ge_3O_{12}$ Phosphor with Near-Infrared Long-Lasting Phosphorescence and Upconversion Luminescence. *Inorg. Chem.* **2014**, *53*, 8638-8645.

(31) Gourier, D.; Bessière, A.; Sharma, S. K.; Binet, L.; Viana,B.; Basavaraju, N.; Priolkarb, K. R. Origin of the Visible Light Induced Persistent Luminescence of Cr^{3+}-Doped Zinc Gallate. *J. Phys. Chem. Solids* **2014**, *75*, 826-837.

(32) van Gorkom, G. G. P.; Henning, J. C. M.; van Stapele, R. P. Optical Spectra of Cr^{3+} Pairs in the Spinel $ZnGa_2O_4$. *Phys. Rev. B* **1973**, *8*, 955–973.

(33) Ueda, J.; Back, M.; Brik, M.; G.; Zhuang, Y.; Grinberg, M.; Tanabe, S. Ratiometric Optical Thermometry Using Deep Red Luminescence from $^4T_2$ and ^2E States of Cr^{3+} in $ZnGa_2O_4$ Host. *Opt. Mater.* **2018**, *85*, 510-516.

(34) Bessière, A.; Sharma, S. K.; Basavaraju, N.; Priolkar,K.R.; Binet,L.; Viana, B.; Bos, A. J. J.; Maldiney, T.; Richard, C.; Scherman, D.; Gourier, D. Storage of Visible Light for Long-Lasting Phosphorescence in Chromium-Doped Zinc Gallate. *Chemistry of Materials* **2014**, *26*, 1365–1373 .

(35) De Vos, A.; Lejaeghere, K.; Vanpoucke, D. E. P.; Joos, J. J.; Smet, P. F.; Hemelsoet, K. First-Principles Study of Antisite Defect Configurations in $ZnGa_2O_4$:Cr Persistent Phosphors. *Inorg. Chem.* **2016**, *55*, 2402–2412.

Table of content:

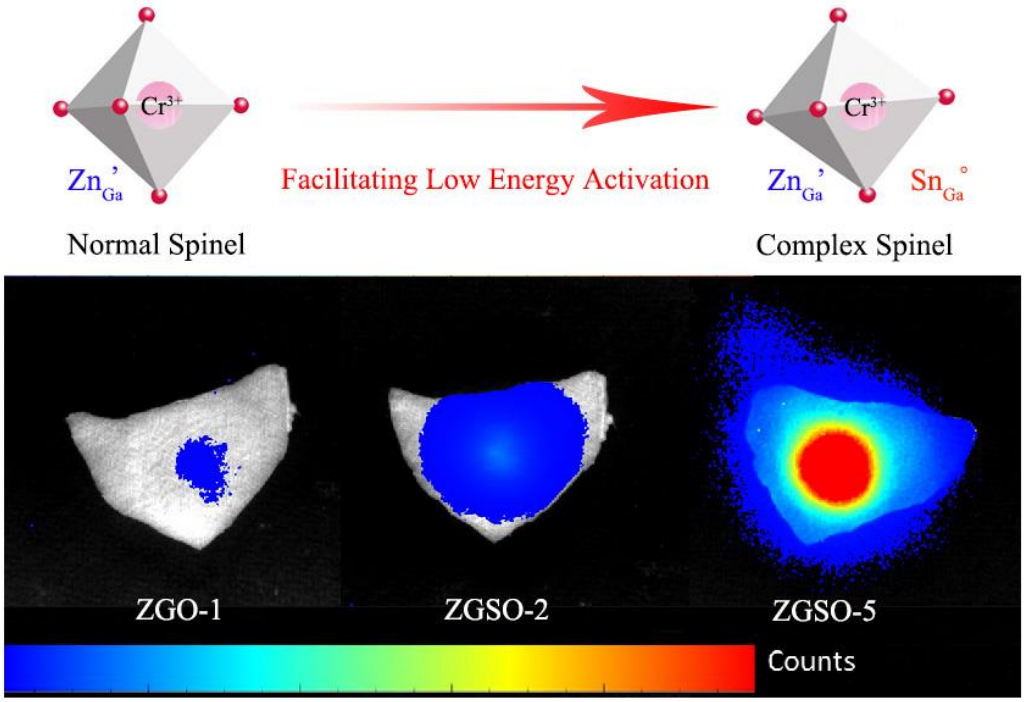

New complex spinel with tin substitution $Zn_{1+x}Ga_{2-2x}Sn_xO_4:Cr^{3+}$ was synthesized with a large increase of the total light storage capability. Both the persistent luminescence excitation and emission spectra of the optimized complex spinel samples are redshifted, which is of interests for easier deep tissues penetration and facilitates the low energy activation.

SI Supplementary Informations

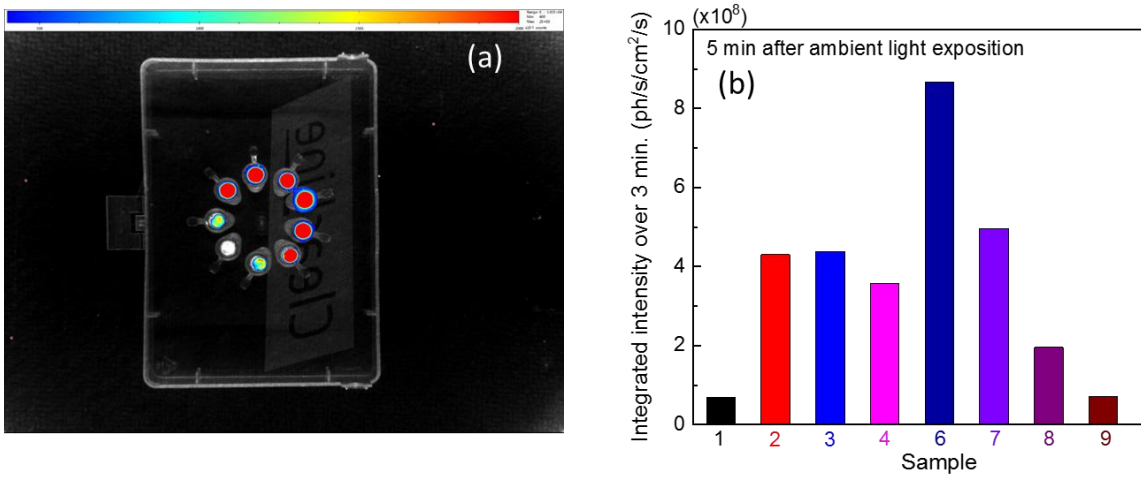

Figure S1: (a) Picture of the samples with photon counting 5 min after ambient lab light exposition (b) the diagram represent the persistent luminescence intensity integrated during 3 min 5 min after ambient lab light exposition.

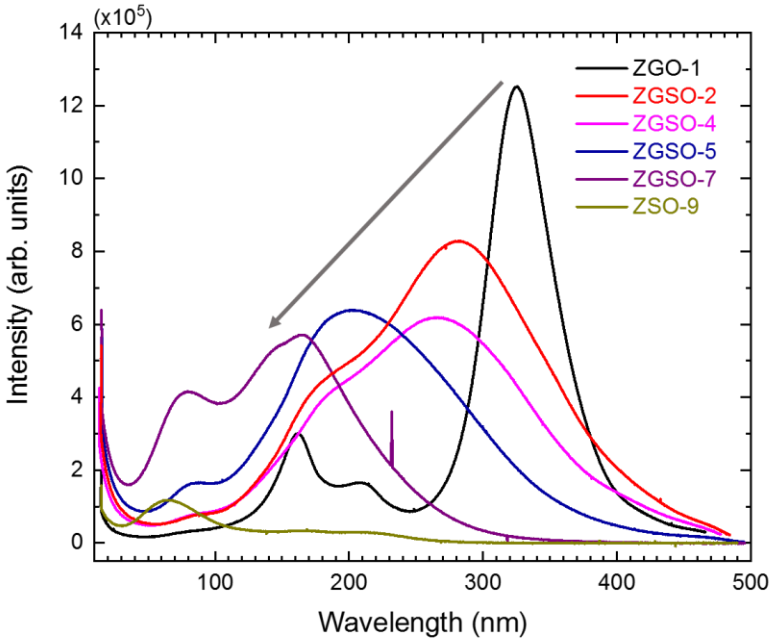

Figure S2: Thermoluminescence glow curves of selected samples recorded after UV excitation during 5 minutes at 14 K.

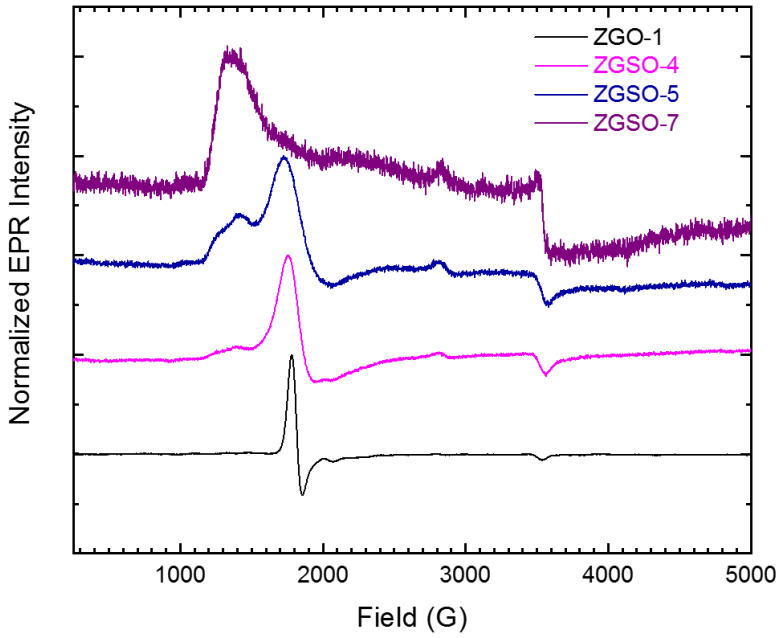

Figure S3: EPR Q band spectra of ZGO-1, ZGSO-4, ZGSO-6 and ZGSO-8 compounds.

In the above figure the effect of the Cr^{3+} surrounding by Sn^{4+} substitution for Ga^{3+} is clearly observable.